

LONG-TERM COLLISIONAL EVOLUTION OF DEBRIS DISKS

TORSTEN LÖHNE AND ALEXANDER V. KRIVOV

Astrophysikalisches Institut und Universitätssternwarte, Friedrich Schiller University Jena, 07745 Jena, Germany; tloehne@astro.uni-jena.de, krivov@astro.uni-jena.de

AND

JENS RODMANN

SCI-SA, Research and Scientific Support Department of ESA, ESTEC, 2200 AG Noordwijk, Netherlands; jrodmann@rssd.esa.int

Received 2007 August 1; accepted 2007 October 22

ABSTRACT

IR surveys indicate that the dust content in debris disks gradually declines with stellar age. We simulated the long-term collisional depletion of debris disks around solar-type (G2 V) stars with our collisional code. The numerical results were supplemented by, and interpreted through, a new analytic model. General scaling rules for the disk evolution are suggested. The timescale of the collisional evolution is inversely proportional to the initial disk mass and scales with radial distance as $r^{4.3}$ and with eccentricities of planetesimals as $e^{-2.3}$. Further, we show that at actual ages of debris disks between 10 Myr and 10 Gyr, the decay laws of the dust mass and the total disk mass are different. The reason is that the collisional lifetime of planetesimals is size dependent. At any moment, there exists a transitional size, which separates larger objects that still retain the “primordial” size distribution set in the growth phase from smaller objects whose size distribution is already set by disruptive collisions. The dust mass and its decay rate evolve as that transition affects objects of ever larger sizes. Under standard assumptions, the dust mass, fractional luminosity, and thermal fluxes all decrease as t^ξ with $\xi = -0.3$ to -0.4 . Specific decay laws of the total disk mass and the dust mass, including the value of ξ , largely depend on a few model parameters, such as the critical fragmentation energy as a function of size, the primordial size distribution of largest planetesimals, and the characteristic eccentricity and inclination of their orbits. With standard material prescriptions and a distribution of disk masses and extents, a synthetic population of disks generated with our analytic model agrees quite well with the observed *Spitzer* MIPS statistics of 24 and 70 μm fluxes and colors versus age.

Subject headings: circumstellar matter — planetary systems: formation

1. INTRODUCTION

Since the *IRAS* discovery of the excess infrared emission around Vega by Aumann et al. (1984), subsequent infrared surveys with *ISO*, *Spitzer*, and other instruments have shown the Vega phenomenon to be common for main-sequence stars. The observed excess is attributed to second-generation circumstellar dust, produced in a collisional cascade from planetesimals and comets down to smallest grains that are blown away by the stellar radiation. While the bulk of such a debris disk’s mass is hidden in invisible parent bodies, the observed luminosity is dominated by small particles at dust sizes. Hence, the studies of dust emission offer a natural tool to gain insight into the properties of planetesimal populations as well as planets that may shape them and, ultimately, into the evolutionary history of circumstellar planetary systems.

In recent years, various photometric surveys of hundreds of nearby stars have been conducted with the *Spitzer Space Telescope*. These are the GTO survey of FGK stars (Beichman et al. 2005, 2006b; Bryden et al. 2006), the FEPS Legacy project (Meyer et al. 2004; Kim et al. 2005), the A star GTO programs (Rieke et al. 2005; Su et al. 2006), the young cluster programs (Gorlova et al. 2006), and others. These observations were done mostly at 24 and 70 μm with the MIPS photometer, but also between 5 and 40 μm with the IRS spectrometer (Jura et al. 2004; Chen et al. 2006). Based on these studies, about 15% of mature solar-type (F0–K0) stars have been found to harbor cold debris disks at 70 μm . For cooler stars, the fraction drops to 0%–4% (Beichman et al. 2006b). For earlier spectral types, the proportion increases to about 33% (Su et al. 2006). At 24 μm , the fraction of systems with detected excess stays similar for A stars but appreciably de-

creases for FGK ones. Similar results in the submillimeter range are expected to become available soon from a survey with SCUBA and SCUBA2 on JCMT (Matthews et al. 2007). Preliminary SCUBA results for M dwarfs suggest, in particular, that the proportion of debris disks might actually be higher than suggested by *Spitzer* (Lestrade et al. 2006).

All authors point out a decay of the observed infrared excesses with systems’ age. However, the values reported for the slope of the decay, assuming a power-law dependence $t^{-\alpha}$, span a wide range. Greaves & Wyatt (2003) suggest $\alpha \lesssim 0.5$, Liu et al. (2004) give $0.5 < \alpha < 1.0$, Spangler et al. (2001) report $\alpha \approx 1.8$, and Greaves (2005) and Moór et al. (2006) derive $\alpha \approx 1.0$. Fits of the upper envelope of the distribution of luminosities over the age yield $\alpha \approx 1.0$ as well (Rieke et al. 2005). Besides, the dust fractional luminosity exhibits a large dispersion at any given age.

In an attempt to gain theoretical understanding of the observed evolution, Dominik & Decin (2003) assumed that equally sized “comets” produce dust through a cascade of subsequent collisions among ever smaller objects. If this dust is removed by the same mechanism, the steady state amount of dust in such a system is proportional to the number of comets. This results in an $M/M_0 \approx \tau/t$ dependence for the amount of dust and for the number of comets or the total mass of the disk. Under the assumption of a steady state, this result is valid even for more complex systems with continuous size distributions from planetesimals to dust. Tenuous disks, where the lifetime of dust grains is not limited by collisions but by transport processes like the Poynting-Robertson drag (Artymowicz 1997; Krivov et al. 2000; Wyatt 2005), follow $M \propto t^{-2}$ rather than $M \propto t^{-1}$.

More recently, Wyatt et al. (2007a) lifted the most severe simplifying assumption of the Dominik-Decin model, that of equal-sized parent bodies, and included them into the collisional cascade. A debris disk they consider is no longer a two-component system “comets+dust.” Instead, it is a population of solids with a continuous size distribution, from planetesimals down to dust. A key parameter of the description by Dominik & Decin (2003) is the collisional lifetime of comets, τ . Wyatt et al. (2007a) replaced it with the lifetime of the largest planetesimals and worked out the dependencies on this parameter in great detail. Since the collisional timescale is inversely proportional to the amount of material, $\tau \propto 1/M_0$, the asymptotic disk mass becomes independent of its initial mass. Only dynamical quantities, i.e., the disk’s radial position and extent, the orbiting objects’ eccentricities and inclinations, and material properties, i.e., the critical specific energy and the disruption threshold, as well as the type of the central star, determine the very long term evolution.

Still, there are two important simplifications made in the model by Wyatt et al. (2007a): (1) the disk is assumed to be in collisional equilibrium at all sizes, from dust up to the largest planetesimals; and (2) the minimum specific energy needed to disrupt colliding objects is independent of their size. As a consequence of assumptions 1 and 2, the size distribution of solids is a single power law. To check how reasonable these assumptions are, realistic simulations of the disks with collisional codes are necessary (e.g., Thébault et al. 2003; Krivov et al. 2005, 2006; Thébault & Augereau 2007).

The aim of this paper is twofold. First, we follow the evolution of debris disks with our elaborate numerical code (Krivov et al. 2005, 2006) to check the existing analytic models and the assumptions 1 and 2 they are based on. Second, in order to make these numerical results easier to use, we develop a new analytic model for the evolution of disk mass and dust mass that relaxes both assumptions 1 and 2 above.

In § 2 we summarize the basic ideas and assumptions and describe our numerical model and the runs of the collisional code. In § 3 the numerical results are presented and dependencies of the collisional timescale on the disk mass, distance to the star, and mean eccentricity of parent bodies are derived. In § 4 the analytic model for the evolution of disk mass and dust mass is developed. In § 5 we analyze the evolution of dust luminosities. In § 6 we use the analytic model to synthesize representative populations of debris disks and compare them with statistics of debris disks derived from the *Spitzer* surveys. A summary is given and conclusions are drawn in § 7.

2. NUMERICAL MODEL AND DESCRIPTION OF RUNS

2.1. Basic Approach

For all numerical runs in this paper, we use a C++-based collisional code (ACE, Analysis of Collisional Evolution). The code numerically solves the Boltzmann-Smoluchowski kinetic equation to evolve a disk of solids in a broad range of sizes (from sub-micrometers to about a hundred kilometers), orbiting a primary in nearly Keplerian orbits (gravity+direct radiation pressure+drag forces) and experiencing disruptive collisions. Collisions are simulated with available material- and size-dependent scaling laws for fragmentation and dispersal in both strength and gravity regime. The current version implements a three-dimensional kinetic model, with masses, semimajor axes, and eccentricities as phase-space variables. This approach automatically enables a study of the simultaneous evolution of mass, spatial, and velocity distribution of particles. The code is fast enough to easily follow the evolution of a debris disk over gigayear timescales. A detailed description of our approach, its numerical implementation, and

astrophysical applications can be found in our previous papers (Krivov et al. 2000, 2005, 2006).

2.2. Disruption Threshold and Critical Specific Energy

An object is said to be disrupted in a collision if the largest fragment is at most half as massive as the original object. If the impactor’s relative velocity is so high that the ratio of impact energy and target mass exceeds the target’s critical specific energy, Q_D^* , the target (and the impactor) is disrupted. For small objects, this binding energy is dominated by material strength, and for larger objects, self-gravity takes over. Both regimes are usually described by a sum of two power laws (Krivov et al. 2005, § 5.1, and references therein)

$$Q_D^* = A_s \left(\frac{s}{1 \text{ m}} \right)^{3b_s} + A_g \left(\frac{s}{1 \text{ km}} \right)^{3b_g}, \quad (1)$$

where “ s ” and “ g ” stand for strength and gravity, respectively. The reported values of the coefficients A_s and A_g vary by more than 1 order of magnitude, and we took $A_s = A_g = 5 \times 10^6 \text{ ergs g}^{-1}$, in agreement with the reference case for basalt given by Benz & Asphaug (1999). The exponents are $3b_s = -0.3$ and $3b_g = 1.5$ (corresponding to -0.1 and 0.5 in the mass scaling). With these parameters, the two power-law components contribute equally at $s \approx 316 \text{ m}$, and the lowest binding energy, the minimum Q_D^* , is reached at $s \approx 129 \text{ m}$. The influence of the choice of parameters on the resulting evolution is discussed in § 4.

For computational reasons, we refrained from including a treatment of cratering collisions in the runs. Note that these were not taken into account in previous studies of the long-term evolution of debris disks (e.g., Dominik & Decin 2003; Wyatt et al. 2007a) either. Thébault et al. (2003) and Thébault & Augereau (2007), who focused on shorter time spans, did include this nondisruptive type of collisions that lead to the continuous erosion of a target by small impacting projectiles. They found the effect to be dominant for particles in between $100 \mu\text{m}$ and 1 cm for the case of the inner β Pictoris disk, while big, kilometer-sized objects in the gravity regime are mainly lost to disruptive collisions (see Table 4 in Thébault et al. 2003). However, including cratering can lower the lifetime of large objects, especially when relative velocities are low and disruptive collisions are rare. Another caveat is that cratering collisions alter the shape of the wavy size distribution at the lower end (Thébault & Augereau 2007), which affects the observable thermal fluxes.

2.3. Collisional Outcomes

The distribution of sizes and the velocities of fragments in an individual (catastrophic) collision have been subject to studies for decades. Laboratory work was done on high-velocity impacts on scales of millimeters and centimeters (e.g., Fujiwara et al. 1977; Fujiwara 1986; Davis & Ryan 1990). Statistics on the mass distributions of observed asteroidal families and geometrical considerations (Paolicchi et al. 1996; Tanga et al. 1999; Tedesco et al. 2005), as well as gravitohydrodynamic simulations of fragmentation and reaccumulation (Michel et al. 2002), cover the range of larger, kilometer-sized bodies. On small scales, the resulting size distributions show a strong dependence on impact velocity and seem to indicate a turn in the power law at fragment sizes around $\approx 1 \text{ mm}$ (or $\approx 1\%$ of the size of the used targets). The slope for objects above that size is steeper than the one for smaller objects (Davis & Ryan 1990). However, Thébault et al. (2003) found that the ratio of these two slopes and the size at which the slope changes influence simulation results only slightly. On kilometer and larger scales, the fragmentation is influenced by

gravitational reaccumulation of relatively small fragments onto bigger ones. Hence, bigger fragments (~ 100 km) will be overabundant, and conversely, smaller fragments (~ 1 km) will be underabundant, compared to the underlying distribution without gravity. The slopes of the size distribution $n(s) \propto s^{-p}$ of kilometer-sized objects are poorly known. A wide range from $p = 3.5$ up to $p = 9.0$ has been reported. These deviations in the kilometer regime are most probably the severest caveat of the power-law approximation because they are independent of the actual material and caused only by gravity. Nevertheless, we assume that fragments follow a single power-law distribution $n_{\text{frag}}(s) \propto s^{-3.5}$, expecting the influence on the final collisional steady state to be only moderate.

2.4. Commons for All Runs

All disk models presented here are set up around a star of solar mass and luminosity. Parameters of the central star affect the disk evolution in various ways. They determine the size limit for grain blowout by radiation pressure and orbital velocities at a given distance, thereby altering impact velocities and rates. For late-type stars, strong stellar winds may affect the dust dynamics (Augereau & Beust 2006; Strubbe & Chiang 2006). On the observational side, dust temperatures and brightnesses are influenced. Here we focus on the scalings for a fixed spectral type (G2 V), and not on scalings between different types.

The disks themselves all share the same material properties and shapes. We adopt the material, described by a bulk density $\rho = 2.5 \text{ g cm}^{-3}$, the radiation pressure efficiency of astronomical silicate (Laor & Draine 1993), and a critical fragmentation energy as specified in § 2.2. We switched off the Poynting-Robertson effect, which is unimportant for debris disks under study, as well as stellar wind drag, which plays only a minor role around G-type stars. The fragments produced in an individual collision are distributed according to a single power law, $dN \propto s^{-3.5} ds \propto m^{-11/6} dm$. A biggest fragment size is assumed to scale with specific impact energy to the power of 1.24 (for details see Krivov et al. 2006). The initial mass distribution is given by $dN \propto m^{-q}$, with $q = 1.87$, a value that accounts for the modification of the classical Dohnanyi (1969) $q = 1.833$ through the size dependence of material strength (see, e.g., Durda & Dermott 1997). The particle masses range from 4.2×10^{-15} g, corresponding to a radius of 74 nm, to 4.2×10^{21} g, corresponding to 74 km. The stepping between the 60 mass bins is logarithmic with a factor of ≈ 4 between neighboring bins. The initial radial profile of the particle density was given by a slope of the normal optical depth of -1.0 . The initial total mass of each disk was set to $1 M_{\oplus}$ (Earth mass).

2.5. Specifics of Individual Runs

We have made four “nominal” runs, each of which corresponds to a certain radial part of the disk between 7.5 and 120 AU from the star (Table 1). In these runs we assumed initial eccentricities of planetesimals to be uniformly distributed between $e_{\min} = 0.0$ and $e_{\max} = 0.3$, spanning three bins centered at 0.05, 0.15, and 0.25. In addition, three runs with altered maximum eccentricity of 0.1, 0.2, and 0.4 were made for the 15–30 AU ring. In all the runs, we assumed that orbital inclinations are distributed between $I_{\min} = e_{\min}/2$ and $I_{\max} = e_{\max}/2$ in accordance with the energy equipartition relation $I = e/2$.

3. NUMERICAL RESULTS AND SCALING LAWS

3.1. Evolution of Disks of Different Masses

A debris disk is said to be in a quasi-steady state or quasi-equilibrium if the amounts of particles with different sizes on

TABLE 1
DESCRIPTION OF NUMERICAL RUNS

Run	Distance (AU)	e_{\max}
Nominal Runs		
ii-0.3.....	7.5–15	0.3
i-0.3.....	15–30	0.3
o-0.3.....	30–60	0.3
oo-0.3.....	60–120	0.3
Additional Runs		
i-0.1.....	15–30	0.1
i-0.2.....	15–30	0.2
i-0.4.....	15–30	0.4

different orbits, while changing with time (therefore “quasi”), stay constant relative to each other. For brevity, we often omit “quasi” and use simply “steady state” or “equilibrium.” To express the condition of a quasi-steady state formally, we can introduce a phase space, in which a dynamical state of each particle is characterized by a vector \mathbf{p} . That vector may be composed, for instance, of coordinates and velocity components. Alternatively, \mathbf{p} may represent the set of orbital elements of the object. Let $n(\mathbf{p}, s, t)$ be the number of objects with radii in $[s, s + ds]$ at phase-space “positions” $[\mathbf{p}, \mathbf{p} + d\mathbf{p}]$ that the disk contains at the time instant t . The assumption of a quasi-steady state can now be expressed as

$$n(\mathbf{p}, s, t) = \tilde{n}(\mathbf{p}, s)f(t). \quad (2)$$

The total disk mass,

$$M_{\text{disk}}(t) = \int \int n(\mathbf{p}, s, t) d\mathbf{p} ds, \quad (3)$$

can be rewritten as

$$M_{\text{disk}}(t) = f(t) \int \int \tilde{n}(\mathbf{p}, s) d\mathbf{p} ds \quad (4)$$

or, setting $f(0) = 1$,

$$M_{\text{disk}}(t) = f(t)M_0, \quad (5)$$

where M_0 is the initial disk mass. As long as objects are both created and lost in two-particle collisions, their gain and loss rates are given by

$$\begin{aligned} \dot{n}(\mathbf{p}, s, t) = & \int \int \int [G(\mathbf{p}, s, \mathbf{p}_1, s_1, \mathbf{p}_2, s_2) \\ & - L(\mathbf{p}_1, s_1, \mathbf{p}_2, s_2)\delta(\mathbf{p} - \mathbf{p}_1)\delta(s - s_1)] \\ & \times \tilde{n}(\mathbf{p}_1, s_1)f(t)\tilde{n}(\mathbf{p}_2, s_2)f(t) d\mathbf{p}_1 ds_1 d\mathbf{p}_2 ds_2, \end{aligned} \quad (6)$$

where the function $G(\mathbf{p}, s, \mathbf{p}_1, s_1, \mathbf{p}_2, s_2)$ describes the gain in population \mathbf{p}, s due to collisions between \mathbf{p}_1, s_1 and \mathbf{p}_2, s_2 and the function $L(\mathbf{p}_1, s_1, \mathbf{p}_2, s_2)$ accounts for the loss in population \mathbf{p}_1, s_1 in collisions with \mathbf{p}_2, s_2 . The disk mass changes at a rate

$$\dot{M}_{\text{disk}}(t) = \int \int \dot{n}(\mathbf{p}, s, t) d\mathbf{p} ds \quad (7)$$

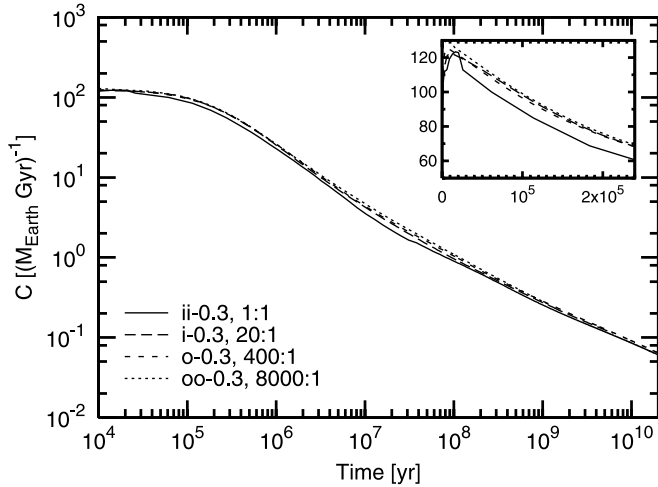


FIG. 1.— Coefficient C from eq. (11) as a function of time for four nominal runs. The total disk mass and time in the runs are scaled according to $M_{\text{disk}} \propto t^{-1}$ to compensate for the difference in dynamical timescale. Note that the near constancy of C at the beginning of the evolution is an artifact of the double-logarithmic plotting. The double-linear inset shows that the decrease of C is *fastest* at earlier times.

or

$$\dot{M}_{\text{disk}}(t) = \dot{f}(t) \int \int \tilde{n}(\mathbf{p}, s) d\mathbf{p} ds. \quad (8)$$

From equations (6) and (7), we find that $\dot{M}_{\text{disk}}(t) \propto f^2(t)$, while equation (8) suggests $\dot{M}_{\text{disk}}(t) \propto \dot{f}(t)$. Hence, $\dot{f}(t) \propto f^2(t)$. Integration yields

$$f = \frac{1}{1 + t/\tau}. \quad (9)$$

Using equation (5), we obtain

$$M_{\text{disk}}(t) = \frac{M_0}{1 + t/\tau}, \quad (10)$$

$$\dot{M}_{\text{disk}}(t) = -CM_{\text{disk}}^2, \quad (11)$$

where $1/C = M_0\tau$, i.e., the product of the initial mass and a characteristic time. This relation is invariant under the transformation $(t, M_{\text{disk}}) \rightarrow (tx, M_{\text{disk}}/x)$, even if C is not constant. Therefore, the mass scale of a system under collisional evolution is inversely proportional to its timescale. For example, doubling the initial total mass halves the collisional lifetime of the system. All curves in the $M_{\text{disk}}(t)$ plots can be shifted along lines of equal tM_{disk} .

Dominik & Decin (2003) used this approach and equated the characteristic time τ with the collisional lifetime of their “comets.” At the initial phase $t \ll \tau$, equation (10) gives

$$M_{\text{disk}}(t) \approx M_0(1 - t/\tau). \quad (12)$$

If the system is old enough so that $t \gg \tau$, the total mass will be just proportional to t^{-1} . Particles whose lifetimes are independent of the total mass are exempt from the asymptotic one-over- t behavior. Examples would be the β -meteoroids that are blown out and small particles in disks tenuous enough for the Poynting-

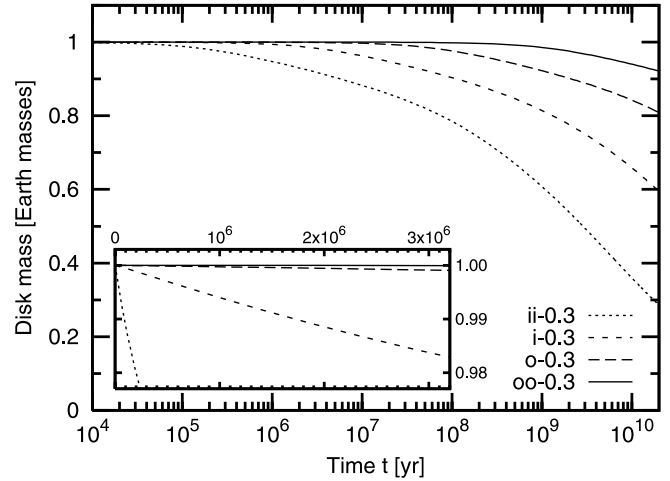


FIG. 2.— Evolution of the total mass in the four nominal runs. Again, the plateau at the beginning of the evolution is an artifact of the logarithmic plotting of time. In fact, the mass decay is strongest at the very beginning (see inset and eqs. [10] and [12]).

Robertson effect to be more efficient than collisions. The total mass of such particles is $\propto t^{-2}$ (Dominik & Decin 2003).

As we have shown, for the systems that undergo a steady state collisional evolution, the factor C in equation (11) (or τ) should be constant. To check this, we evaluated $C = -\dot{M}_{\text{disk}}/M_{\text{disk}}^2$ for every two subsequent time steps of the numerical runs. The results are given in Figure 1.

Instead of being constant at later times, C decreases, roughly following a power law $C \propto t^{-2/3}$ to $t^{-4/5}$. The explanation is simple: the systems did not reach an equilibrium where $t \gg \tau$ or at least $t \approx \tau$ during their lifetime. The evolution of the total mass in Figure 2 demonstrates that as well.

3.2. Dependence on Distance from the Star

Rings of identical mass but at different distances have different collisional timescales. The comparison in Figure 1 shows that doubling the distance requires a 20-fold increase in disk mass to have the same timescale. This corresponds to a power-law dependence

$$C \propto r^{-4.3}. \quad (13)$$

In a thorough analytic approach based on a Dohnanyi-type collisional cascade, Wyatt et al. (2007a) came up with $C \propto r^{-13/3}$, which is in good agreement with our numerical result. This index is made up of three contributions. First, the density in the rings drops with r^{-3} as their circumference, height, and width increase linearly. Second, the relative velocities have an $r^{-1/2}$ dependence. Third, these impact velocities affect the minimum required mass for a projectile to be disruptive and thereby the total number of such projectiles. That gives another r^{-1-q} , where q is the slope in the appropriate mass distribution, e.g., $q = 11/6$ for the classical Dohnanyi case. See § 4.3 for details.

3.3. Dependence on Eccentricities of Parent Bodies

The intrinsic collisional probability of planetesimals is nearly independent of their eccentricities, as long as they are not too high (see, e.g., Krivov et al. 2006). Nevertheless, eccentricities determine impact velocities and, through that, the minimum size of a disruptive projectile. Therefore, higher planetesimal eccentricities imply a larger rate of catastrophic collisions and thus a faster collisional evolution. To quantify the dependence, we have made runs with maximum eccentricities of 0.1, 0.2, 0.3, and 0.4 (Table 1)

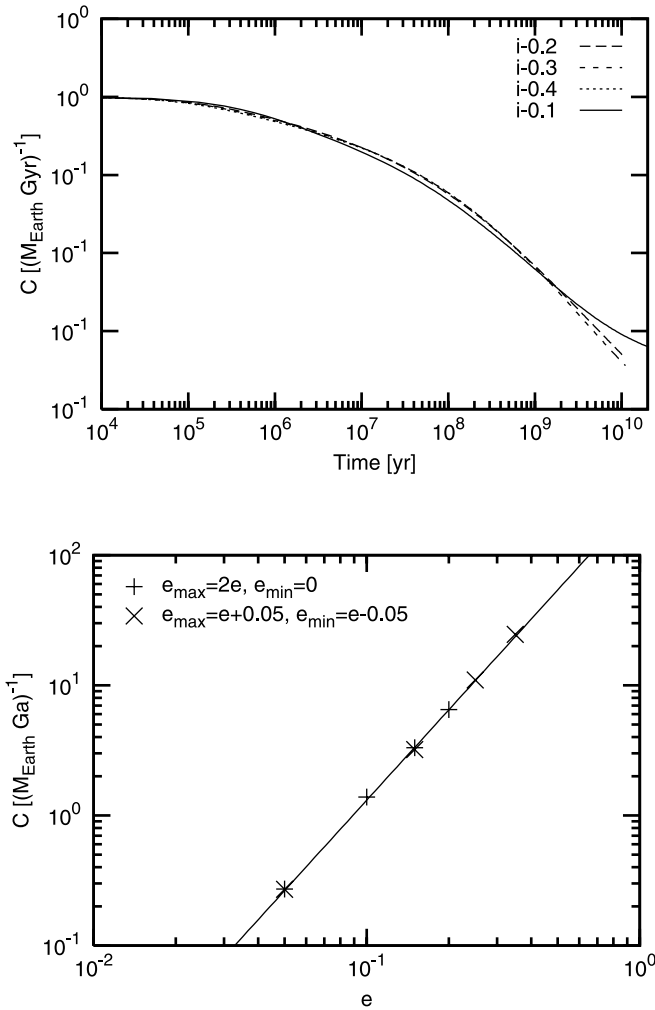


FIG. 3.—Influence of the average eccentricity of planetesimals on the timescale of the disk’s collisional evolution. *Top*: Evolution of the parameter C from eq. (11) for four different runs (i-0.1, . . . , i-0.4). *Bottom*: Four initial C -values vs. average eccentricity $e = (e_{\max} + e_{\min})/2$ (plus signs) together with the $C \propto e^{9/4}$ fit for those runs (solid line) and the same for runs with a narrower range of eccentricities, as described in § 3.3 (crosses).

and determined the values of C . The results suggest a power law $C \propto e_{\max}^{9/4}$ as shown in Figure 3.

This result comes as a surprise. Wyatt et al. (2007a) derive $C \propto e^{5/3}$. The same scaling is inherited by our analytic model (see eq. [36]). Since this discrepancy can be due either to an incompleteness of the analytic approach or to a nonlinear relation between the maximum and the effective eccentricity, we tried to rule out the latter case by performing additional runs with e confined to narrow bins of width 0.1, centered at 0.05, 0.15, 0.25, and 0.35. These runs can be well described by the same power law, $C \propto e^{9/4}$ (Fig. 3). Therefore, the analytic model fails to reproduce this particular dependence. Nevertheless, it correctly describes many others, as the next sections show.

4. ANALYTIC MODEL FOR EVOLUTION OF DISK MASS AND DUST MASS

4.1. Size and Mass Distributions

In what follows, we analyze size or mass distributions of objects. Different authors use distributions of different physical quantities (number, cross section, mass) with different arguments (particle size or mass) and of different type (differential, cumulative, per

size decade, etc.). A standard choice is to use a differential size distribution, $n(s)$, that gives the number of particles per unit size interval,

$$n(s) \equiv \int n(\mathbf{p}, s) d\mathbf{p}, \quad (14)$$

or a differential mass distribution, $n(m)$, that gives the number of particles per unit mass interval. Instead of n , it is often convenient to use the mass-per-size-decade distribution,

$$\frac{dM_{\text{disk}}}{d \log_{10} s} = \ln(10) s m(s) n(s). \quad (15)$$

In contrast to $n(s)$, this quantity tells us directly in which size range objects contribute the most to the mass of the system. Therefore, we use it when plotting size or mass distributions.

In the case of a power-law size distribution, $n(s) ds \propto s^{2-3q} ds$ is the number of objects with sizes $[s, s + ds]$ and $n(m) dm \propto m^{-q} dm$ is the number of objects with masses $[m, m + dm]$. The mass per size decade is $\propto s^{6-3q} \propto m^{2-q}$. When $q < 2$, the total mass is determined by large bodies, whereas the cross section is dominated by small particles as long as $q > 5/3$.

4.2. Three-Slope Distribution

The combination of material strength at smaller sizes and self-gravity at larger ones, with a turnover at around 100 m, causes the size distribution in a collisionally evolving system to strongly deviate from a single-slope power law, especially for object sizes of around 1 km. This is illustrated by Figure 4, which shows how a disk evolves from the first-guess power law to a more realistic size distribution. The speed of this evolution is determined by the collisional timescales of populations of different-sized particles in the disk. Populations of smaller particles with sufficiently short lifetimes consist mostly of fragments of disruption of larger bodies. They will have reached collisional equilibrium with each other soon, according to their production rate by populations with longer lifetimes. The latter populations of bigger particles will still be on their way to a steady state. As time goes by, more and more long-lived populations will undergo the transition from primordial to reprocessed material.

As this transitional mass moves toward larger objects with time, the smaller particles follow to a new “intermediate steady state.” The bottom panel of Figure 4 shows the development of the characteristic wavy shape in the size distribution (e.g., Campo Bagatin et al. 1994; Thébault et al. 2003; Krivov et al. 2006) at the small-size end near the blowout limit due to radiation pressure. Once established, this shape remains constant. Only the absolute level changes because this distribution at smaller sizes acts as the trail of the distribution at larger sizes. In the top panel of Figure 4, the number of smaller particles is constant for some time and then goes down, as soon as the distribution in the gravity regime starts to deviate from its primordial one.

These arguments suggest that an overall size distribution $n(s)$ can be approximated by a combination of three power laws (Fig. 5). For particles large enough to be only barely affected by collisions at time t , we assume n to follow s^{2-3q_p} . Here q_p is the “primordial” slope determined by the processes in which these planetesimals have formed. Small particles that are in quasi-steady state are separated from bigger primordial objects by a transition zone that we characterize by a time-dependent size $s_t(t)$. To distinguish between the strength and gravity regimes, we introduce two more power laws and assume the mass distribution to

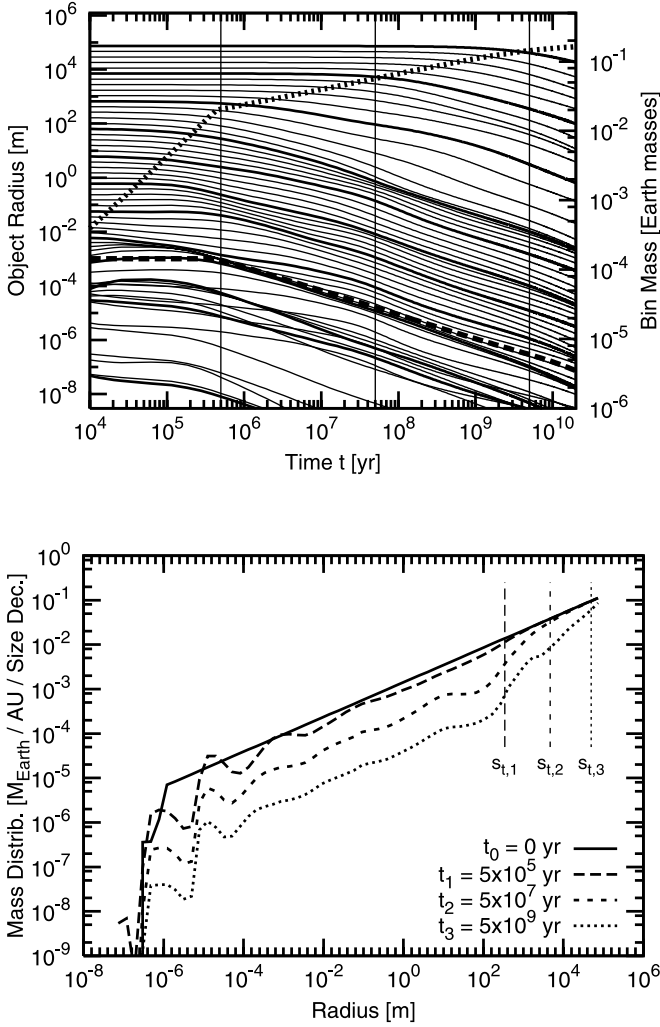


FIG. 4.—Results of the ii-0.3 run. *Top*: Time evolution of mass in individual mass bins, from the largest bodies of 74 km in radius to the smallest, 74 nm in radius. The mass ratio between adjacent bins is 4. Each solid line corresponds to one individual bin and gives the mass contained in that bin (see the right axis) as a function of time. The left axis can be used to find the line that corresponds to a given object size. The thick dashed line corresponds to ≈ 1 mm radius, i.e., to the largest solids still treated as dust. The thick dotted line, which goes roughly through the turning points of the lines, is the transition size $s_t(t)$; see eq. (37). *Bottom*: Size/mass distribution at four specific instants of time shown in the top panel with vertical lines: initially, after 5×10^5 yr when s_t has reached s_b , and after 5×10^7 and 5×10^9 yr when significant dust depletion has already occurred.

follow $n \propto s^{2-3q_g}$ for gravity-dominated quasi-steady state and $n \propto s^{2-3q_s}$ for strength-dominated quasi-steady state. The two regimes are separated by an object size s_b , which we call the “breaking radius.” Thus, the waviness is neglected, but the effect of a size-dependent Q_D^* is kept.

The resulting size distribution is given by

$$n(s) = n_{\max} \left(\frac{s_{\max}}{s} \right)^{3q_p-2}, \quad s_t \leq s < s_{\max}, \quad (16)$$

$$n(s) = n_{\max} \left(\frac{s_{\max}}{s_t} \right)^{3q_p-2} \left(\frac{s_t}{s} \right)^{3q_g-2}, \quad s_b \leq s < s_t, \quad (17)$$

$$n(s) = n_{\max} \left(\frac{s_{\max}}{s_t} \right)^{3q_p-2} \left(\frac{s_t}{s_b} \right)^{3q_g-2} \left(\frac{s_b}{s} \right)^{3q_s-2}, \quad s_{\min} < s < s_b, \quad (18)$$

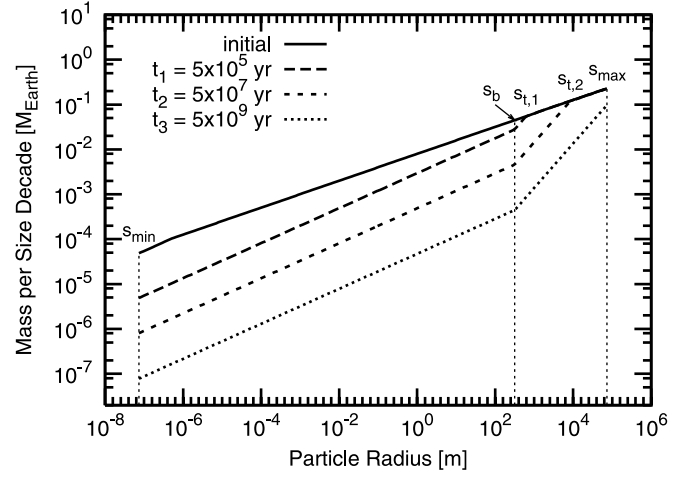


FIG. 5.—Schematic plot of the three regimes in the mass distribution and its time evolution. The mass s_t divides second-generation material in collisional equilibrium ($s < s_t$) from primordial material ($s > s_t$), while s_b divides the material strength regime ($s < s_b$) from the gravity regime ($s > s_b$).

where $n_{\max} \equiv n(s_{\max})$, with s_{\max} being the size of the largest planetesimals. From this distribution, two important quantities can be derived. One is the total *disk* mass,

$$M_{\text{disk}} = \int_{s_{\min}}^{s_{\max}} n(s) \frac{4}{3} \pi \rho s^3 ds, \quad (19)$$

and the other is *dust* mass (which determines the infrared luminosity and therefore provides a link to observations),

$$M_{\text{dust}} = \int_{s_{\min}}^{s_d} n(s) \frac{4}{3} \pi \rho s^3 ds, \quad (20)$$

where $s_{\min} \leq s_d < s_b$.

4.3. Collisional Lifetimes of Planetesimals

As seen from equations (16)–(20), the evolution of M_{disk} and M_{dust} is controlled by $n_{\max}(t)$ and $s_t(t)$.

We start with n_{\max} and assume, according to equations (2) and (9),

$$n_{\max}(t) = \frac{n_{\max}(0)}{1 + t/\tau_{\max}}, \quad (21)$$

where τ_{\max} is the collisional lifetime of these largest bodies. Equation (21) closely reproduces the disk evolution as soon as the whole system has reached the quasi-steady state at all sizes or, in other words, as soon as $s_t(t)$ has reached s_{\max} .

The second quantity that we need, $s_t(t)$, could easily be obtained by inverting the function $\tau(s)$, the collisional lifetime of planetesimals of a given size s . To obtain $\tau(s)$, we begin with the lifetime of the largest objects in a disk. Assuming that $q > 5/3$, Wyatt et al. (2007a, their eq. [12]) approximated it as

$$\tau_{\max} = \frac{4\pi}{\sigma_{\text{tot}}} \left(\frac{s_{\max}}{s_{\min}} \right)^{3q_p-5} \frac{r^{5/2} dr}{(\mathcal{G}M_*)^{1/2} f(e, I) G(q, s)}, \quad (22)$$

where e and I are the effective orbital eccentricities and inclinations, σ_{tot} is the initial cross-sectional area of the disk material, \mathcal{G} is the gravitational constant, r is the radial distance of the ring of parent bodies, and dr is its width. The slope q in their single

power-law approach corresponds to the primordial slope q_p in our nomenclature. The functions f and G are given by

$$f(e, I) = \sqrt{\frac{5}{4}e^2 + I^2}, \quad (23)$$

$$G(q, s) = \left[X_c(s)^{5-3q} - \left(\frac{s_{\max}}{s} \right)^{5-3q} \right] + 2 \frac{q-5/3}{q-4/3} \left[X_c(s)^{4-3q} - \left(\frac{s_{\max}}{s} \right)^{4-3q} \right] + \frac{q-5/3}{q-1} \left[X_c(s)^{3-3q} - \left(\frac{s_{\max}}{s} \right)^{3-3q} \right], \quad (24)$$

with

$$X_c(s) = \left[\frac{2Q_D^*(s)rf(e, I)^{-2}}{\mathcal{G}M_*} \right]^{1/3}. \quad (25)$$

While $f(e, I)$ describes the dependence of the impact velocities on eccentricities and inclinations, the functions G and X_c characterize the disruption of planetesimals by smaller projectiles. Namely, $X_c(s)$ is the minimum size ratio between the smallest disruptive projectile and the target, and $G(q, s)$ is the number of disruptive projectiles.

We need the lifetime of objects of an arbitrary size, $\tau(s < s_{\max})$. To derive it, we can simply substitute s_{\max} by s in equation (22), obtaining

$$\tau(s) = \frac{4\pi}{\sigma_{\text{tot}}} \left(\frac{s}{s_{\min}} \right)^{3q_p-5} \frac{r^{5/2} dr}{(\mathcal{G}M_*)^{1/2}} \frac{I}{fG(q_p, s)}. \quad (26)$$

In order to replace the dependence on the initial cross-sectional area of objects, σ_{tot} , with their initial total mass, M_0 , we need to derive both quantities from the initial size distribution in equation (16). The area is given by

$$\sigma_{\text{tot}} = n_{\max}(0) \frac{\pi s_{\max}^3}{3q_p-5} \left[\left(\frac{s_{\max}}{s_{\min}} \right)^{3q_p-5} - 1 \right]. \quad (27)$$

Since it is dominated by s_{\min} for $q_p > 5/3$, we obtain

$$\sigma_{\text{tot}} = n_{\max}(0) \frac{\pi s_{\max}^3}{3q_p-5} \left(\frac{s_{\max}}{s_{\min}} \right)^{3q_p-5}. \quad (28)$$

The initial total disk mass is

$$M_0 = n_{\max}(0) \frac{4\pi \rho s_{\max}^4}{3(6-3q_p)} \left[1 - \left(\frac{s_{\min}}{s_{\max}} \right)^{6-3q_p} \right]. \quad (29)$$

For $q_p < 2$, it is dominated by s_{\max} . However, since a primordial slope $q_p \geq 2$ is not unrealistic (see § 4.8), we refrain from using a further approximation. Then, the area and the mass are related through

$$\sigma_{\text{tot}} = M_0 \frac{3(2-q_p)}{4(q_p-5/3)} s_{\max}^{-1} \left(\frac{s_{\max}}{s_{\min}} \right)^{3q_p-5} \times \left[1 - \left(\frac{s_{\min}}{s_{\max}} \right)^{6-3q_p} \right]^{-1}. \quad (30)$$

Inserting equation (30) into equation (26) results in

$$\tau(s) = \frac{16\pi\rho}{3M_0} \left(\frac{s}{s_{\max}} \right)^{3q_p-5} \frac{s_{\max} r^{5/2} dr}{(\mathcal{G}M_*)^{1/2}} \times \frac{q_p-5/3}{2-q_p} \left[1 - \left(\frac{s_{\min}}{s_{\max}} \right)^{6-3q_p} \right] \frac{I}{f(e, I)G(q_p, s)}, \quad (31)$$

which gives the collisional lifetime of an object with radius s . Note that

$$\frac{1}{2-q_p} \left[1 - \left(\frac{s_{\min}}{s_{\max}} \right)^{6-3q_p} \right] \rightarrow 3 \ln \frac{s_{\max}}{s_{\min}} \quad (32)$$

for $q_p \rightarrow 2$.

If the mean impact velocities in the system are high enough to allow planetesimals of radius s to get disrupted in a collision, i.e., $X_c(s) \ll s_{\max}/s$, $G(q_p, s)$ reduces to

$$G(q_p, s) \approx \frac{q_p-5/3}{q_p-1} X_c(s)^{3-3q_p}, \quad (33)$$

and $\tau(s)$ to

$$\tau(s) = \frac{16\pi\rho}{3M_0} \left(\frac{s}{s_{\max}} \right)^{3q_p-5} \frac{I r^2 dr}{f(e, I)^{2q_p-1}} \left(\frac{r}{\mathcal{G}M_*} \right)^{q_p-1/2} \times \frac{q_p-1}{2-q_p} \left[1 - \left(\frac{s_{\min}}{s_{\max}} \right)^{6-3q_p} \right] (2Q_D^*)^{q_p-1}. \quad (34)$$

Now, we take into account the dependence of Q_D^* on the object size s , as was done by O'Brien & Greenberg (2003). If we are only interested in the gravity regime, $s > s_b$, equation (1) is simplified to

$$Q_D^*(s) \approx Q_{D,b}^* \left(\frac{s}{s_b} \right)^{3b_g}, \quad (35)$$

where $Q_{D,b}^*$ is the critical specific energy at the breaking radius, i.e., around the minimum of $Q_D^*(s)$. Assuming, further, that $I \propto e$, we can write down the dependencies of the collisional lifetime,

$$\tau(s) \propto \sigma_{\text{tot}}^{-1} s^{3q_p-5+3(q_p-1)b_g} r^{3/2+q_p} dr e^{-5/3}. \quad (36)$$

O'Brien & Greenberg (2003) yield the same size dependence on s in their equation (11).

To find $s_t(t)$, the object size below which a steady state is reached, we assume that the populations move from their primordial state to the quasi-steady state instantaneously when the system age reaches their initial mean collisional lifetime, $\tau(s_t) = t$. Inverting that, the resulting mass of objects in transition can be retrieved as a function of system age. Keeping the assumption $X_c \ll s_{\max}/s$, the relation is

$$s_t(t) \propto t^{1/[3q_p-5+3(q_p-1)b_g]} \quad (37)$$

for $t > \tau(s_b) \equiv \tau_b$. This transitional size is also plotted in Figure 4.

Pan & Sari (2005) followed a similar approach in their study of the Kuiper Belt size distribution. Describing the propagation of the shock wave through the target, they introduce a parameter β that varies between 3/2 (if all energy of a projectile goes to the shock wave) and 3 (if all its momentum does). Their β equals

$1/b_g$ in our nomenclature, and $b_g = 0.5$ leads to $\beta = 2$. In addition, we have to replace their slope q_0 with our $3q_p - 2$. Then, given their equations (6), (7), and $N_{>s} \propto s^{3-3q_p}$, we yield the same exponent as in our equation (37). Note that what Pan & Sari (2005) call “breaking radius” is our “transition radius” s_t , and their “radius of equilibrium” is our “breaking radius” s_b .

4.4. Evolution of Disk Mass

Now, we derive the full expression for the time-dependent total disk mass. Using the size distribution given by equation (18), n_{\max} from equation (21), and expressing $n_{\max}(0)$ through M_0 with the aid of equation (29), we can perform the integration in equation (19). Then, the resulting time-dependent disk mass is

$$M_{\text{disk}}(t) = \frac{M_0}{1 + t/\tau_{\max}} \left[1 - \left(\frac{s_{\min}}{s_{\max}} \right)^{6-3q_p} \right]^{-1} \times \left\{ 1 - \left[\frac{s_t(t)}{s_b} \right]^{6-3q_p} \left(\frac{s_b}{s_{\max}} \right)^{6-3q_p} \left(1 - \frac{2-q_p}{2-q_g} \right) + \left[\frac{s_t(t)}{s_b} \right]^{3q_g-3q_p} \left(\frac{s_b}{s_{\max}} \right)^{6-3q_p} \left(\frac{2-q_p}{2-q_s} - \frac{2-q_p}{2-q_g} \right) - \left[\frac{s_t(t)}{s_b} \right]^{3q_g-3q_p} \left(\frac{s_b}{s_{\max}} \right)^{3q_s-3q_p} \left(\frac{s_{\min}}{s_{\max}} \right)^{6-3q_s} \left(\frac{2-q_p}{2-q_s} \right) \right\} \quad (38)$$

for $\tau_b < t < \tau_{\max}$. To make equation (38) valid for earlier phases, i.e., for $t < \tau_b$, s_b should be replaced by $s_t(t)$. The sizes involved are the maximum object size s_{\max} , the transition size between the primordial and reprocessed material s_t , and the breaking radius between the gravity and strength regime s_b . The lower limit in the size distribution, s_{\min} , is crucial for the dust emission and is usually taken to be the radiation pressure blowout limit. As long as $q_p < 2$, it is fairly unimportant for the mass budget. However, we are interested in $q_p \geq 2$ as well. Therefore, we can safely set $s_{\min} = 0$ only in the last line of equation (38), where it enters through s_{\min}/s_{\max} to the power of $6 - 3q_s$, with $q_s \approx 11/6 < 2$.

The relative importance of the terms in equation (38) is illustrated in Figure 6. A combination of the classic Dominik-Decin behavior in the first line of equation (38) together with the second line is a reasonably accurate approximation to $M_{\text{disk}}(t)$ for most of the time. With the aid of equation (37), equation (38) transforms to

$$M_{\text{disk}}(t) \approx \frac{M_0}{1 + t/\tau_{\max}} \left[1 - \left(\frac{s_{\min}}{s_{\max}} \right)^{6-3q_p} \right]^{-1} \times \left[1 - \left(\frac{s_b}{s_{\max}} \right)^{6-3q_p} \left(\frac{t}{\tau_b} \right)^{(2-q_p)/[q_p-5/3+(q_p-1)b_g]} \times \left(1 - \frac{2-q_p}{2-q_g} \right) \right] \quad (39)$$

for $\tau_b < t < \tau_{\max}$. At $t \ll \tau_{\max}$, and assuming $q_p = 1.87$, a further approximation is

$$M_{\text{disk}}(t) \approx M_0(1 - \text{const } t^{0.2}). \quad (40)$$

The evolution of the disk mass, both from the numerical runs and from the analytic solution given by equation (38), is plotted in Figure 7, showing a good agreement between analytics and numerics. A deviation is only seen around $t = \tau_b$ where the

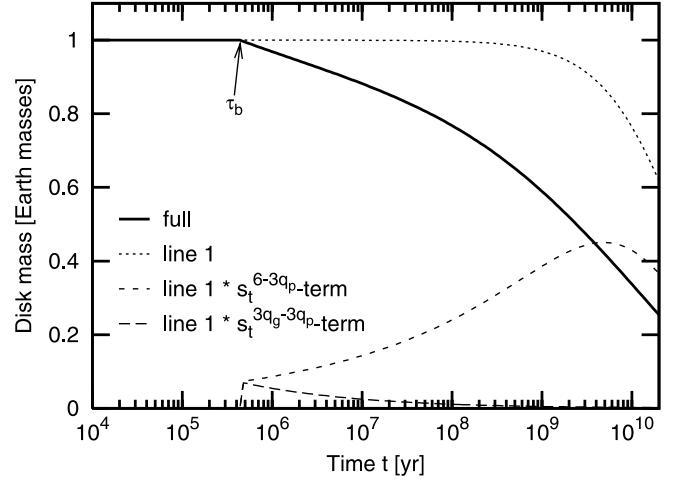


FIG. 6.—Contributions of different terms in eq. (38) (dotted and dashed lines) and their total (solid line).

transition from primordial to reprocessed state sets in for gravity-dominated objects. The reason is that, to ease the analytic treatment, we neglect the smooth natural transition from material strength to self-gravity given by equation (1) and assume a sharp break between the two power laws instead.

4.5. Evolution of Disk Mass at Latest Stages

As soon as the age of the system has reached the collisional lifetime of the largest bodies, i.e., at $t > \tau_{\max}$, the solids of all sizes in the disk reach quasi-steady state, and the change in total mass will be dominated by $1/t$. At this latest phase, the projectiles that can destroy objects of size s_{\max} no longer follow a size distribution with the primordial slope, $2 - 3q_p$. Instead, they have the slope of a collisional cascade under gravity regime, $2 - 3q_g$. The slightly longer collisional lifetime can neither be expressed through equation (22), which uses the initial cross section σ_{tot} , nor through equation (31), which contains the initial disk mass M_0 and slope q_p . The correct way to evaluate τ_{\max} is to use the initial number density of biggest objects, $n_{\max}(0)$, and the slope q_g . Expressing σ_{tot} in equation (22) through n_{\max} with the help of equation (28) and replacing then q_p with q_g , we obtain

$$\tau_{\max} = \frac{12q_g - 20}{n_{\max}(0)s_{\max}^3} \frac{r^{5/2} dr}{(GM_*)^{1/2}} \frac{I}{f(e, I)G(q_g, s_{\max})}. \quad (41)$$

Expressing now $n_{\max}(0)$ through M_0 by virtue of equation (29) yields

$$\tau_{\max} = \frac{16\pi\rho}{3M_0} s_{\max} \frac{r^{5/2} dr}{(GM_*)^{1/2}} \frac{q_g - 5/3}{2 - q_p} \times \left[1 - \left(\frac{s_{\min}}{s_{\max}} \right)^{6-3q_p} \right]^{-1} \frac{I}{f(e, I)G(q_g, s_{\max})}, \quad (42)$$

where both slopes, q_p and q_g , appear (cf. eqs. [22] and [31]).

4.6. Evolution of Mass in Dynamically “Cold” Disks

All the treatment above applies to planetesimal belts where relative velocities are high enough for the biggest objects to be destroyed by mutual collisions. This might not be the case in dynamically “cold” disks with low eccentricities and inclinations and/or very far from the star.

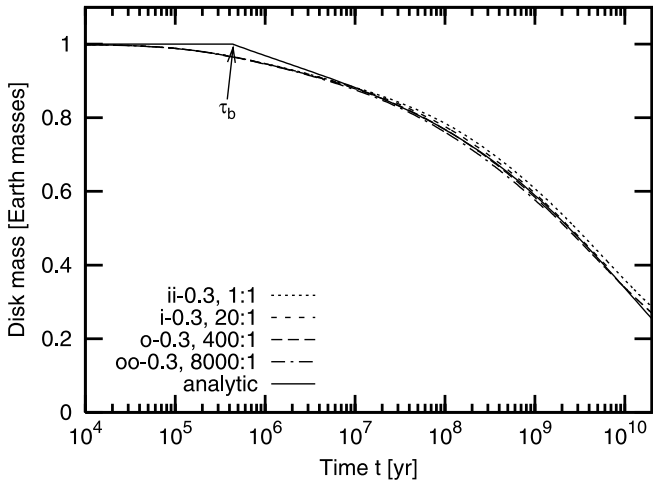


FIG. 7.— Evolution of total masses with (scaled) time, obtained in four numerical runs and with the analytic model.

Consider again the lifetime of objects $\tau(s)$. As s increases, $X_c(s)$ (eq. [25]) increases too and at a certain point reaches s_{\max}/s . At this point, G (eq. [24]) becomes zero and $\tau(s)$ (eq. [31]) goes to infinity. This means that, for a given impact velocity, objects above a certain critical size cannot be disrupted anymore. In systems with low relative velocities, that critical size may happen to be smaller than s_{\max} . This will affect the mass evolution. Specifically, when s_t reaches that critical size, the overall mass decay ceases.

To illustrate such effects, Figure 8 shows the influence of the effective e and I on the evolution of the total mass of a disk of initially $1 M_{\oplus}$ at an effective distance of 10 AU, calculated with our analytic model. For colder disks, the curves start to flatten. This happens because the largest planetesimals (that dominate the total mass) stay intact, which slows down the mass loss.

4.7. Evolution of Dust Mass

The dust mass can be evaluated in a similar way as the disk mass. We use now equations (18), (20), (21), (29), and (37). Neglecting the minimum mass s_{\min} only when it enters the formula through s_{\min}/s_{\max} , we obtain

$$M_{\text{dust}}(t) = \frac{M_0}{1 + t/\tau_{\max}} \left(\frac{t}{\tau_b} \right)^{(q_g - q_p)/(q_p - 5/3 + (q_p - 1)b_g)} \frac{2 - q_p}{2 - q_s} \times \left(\frac{s_b}{s_{\max}} \right)^{2 - q_p} \left[\left(\frac{s_D}{s_b} \right)^{2 - q_s} - \left(\frac{s_{\min}}{s_b} \right)^{2 - q_s} \right]^{-1} \quad (43)$$

for $\tau_b < t < \tau_{\max}$. Before that, i.e., at $t < \tau_b$, we have q_s and b_s instead of q_g and b_g , respectively. If the assumed primordial slope, q_p , equals the steady state slope in the strength regime, q_s , the dust mass stays constant, which is the case for the first part of the numerical integration. However, as soon as the transitional zone reaches objects large enough to be influenced by self-gravity, equation (43) starts to work. It shows that the evolution of dust mass depends most strongly on the difference between q_p and q_g . The dust mass decay, obtained from both the numerical runs and the analytic solution given by equation (43), is shown in Figure 9. For $t > \tau_b$, we roughly have $M_{\text{dust}} \propto t^{\xi}$ with $\xi \approx -0.3$.

We finally note that equation (43) is valid as long as the collisional lifetime of the largest planetesimals is longer than the age of the system. When $t > \tau_{\max}$, t/τ_b in that equation must be replaced by τ_{\max}/τ_b .

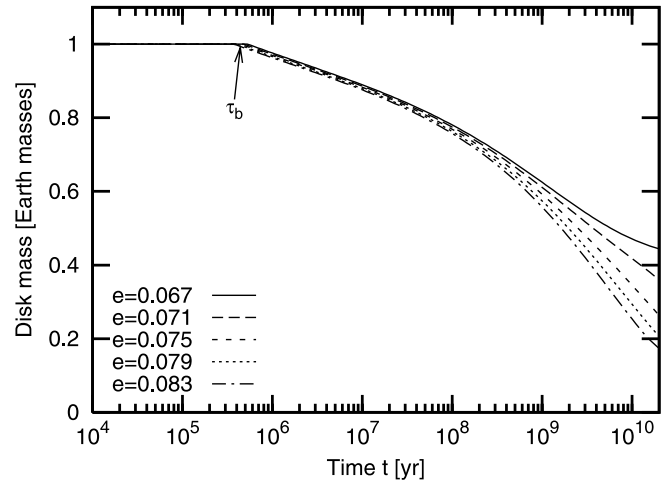


FIG. 8.— Influence of the effective eccentricity assumed in the analytic model for a disk of $1 M_{\oplus}$ at $r = 10$ AU with a radial extent $dr = 7.5$ AU. The $I = e/2$ relation between eccentricity and inclination is assumed.

4.8. The Model Parameters

Our analytic model contains several parameters that either differ from similar parameters in the numerical model (such as e) or are absent there (such as q_s and q_g). To use the analytic model, we have to specify them. We now describe how this can be done, explaining, in particular, the choice of parameters used to plot analytic curves in Figures 6–9.

Two important free parameters of the analytic model are q_s and q_g . We use the work of O'Brien & Greenberg (2003), who found the slope of the size distribution in a system in a collisional steady state. With the dependence of the critical specific energy on the object size given in equation (1), they give a power-law index

$$q = \frac{11/6 + b}{1 + b} \quad (44)$$

in their equation (24). With $b = b_s = -0.1$ for the strength regime, we have $q = q_s = 1.877$. Similarly, with $b = b_g = 0.5$ for the gravity regime, equation (44) can be used to derive $q_g \approx 5/3$. It is these values that we used in equation (38) to produce Figures 6–8 and in equation (43) to plot Figure 9.

In contrast to q_s and q_g , the primordial slope, q_p , is a free parameter not only in the analytic model but also in the numerical

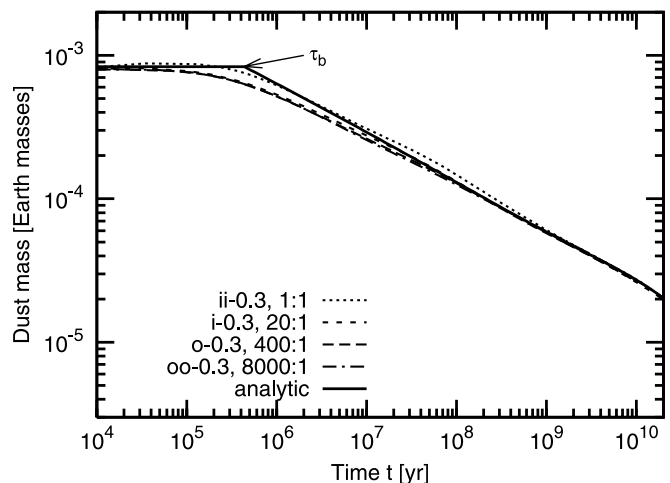


FIG. 9.— Similar to Fig. 7, but for dust masses, i.e., masses in particles with radii below 1 mm.

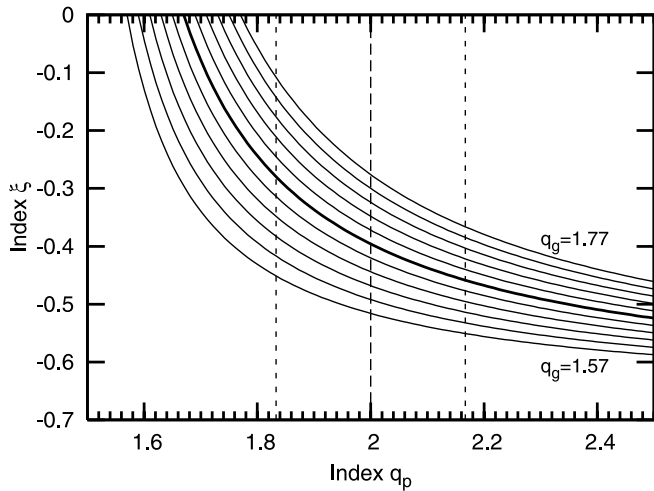


FIG. 10.—Index ξ of the power-law evolution of the dust mass, $M_D \propto t^\xi$. The horizontal axis gives the dependence on the slope of the primordial mass distribution, q_p , for values from $q_g = 1.57$ (bottom) to $q_g = 1.77$ (top) for the slope in the gravity regime. The thick line is for $q_g = 1.67 \approx 5/3$. Vertical lines indicate the mean value and error estimates for q_p from Trujillo et al. (2001).

one. As stated in § 2.4, in all “nominal” runs we assumed $q_p = 1.87$, which corresponds to $p_p = 3q_p - 2 = 3.61$ in the size scaling. In principle, q_p describes the mass distribution at the onset of the collisional grinding of the disk and, therefore, represents a link to the planetesimal formation process. The outcome of the agglomeration phase is the input to the phase of disruptive collisions. The Kuiper Belt is the only source for observational constraints to this parameter so far, and recent surveys suggest a value of $p_p = 4.0 \pm 0.5$ (e.g., Trujillo et al. 2001; Bernstein et al. 2004) or $q_p = 2.00 \pm 0.17$. Simulations by Kenyon & Bromley (2004) yield $p_p = 4.0\text{--}4.5$ or $q_p = 2.00\text{--}2.17$. According to equation (43), where we have $M_{\text{dust}} \propto t^\xi$, and together with $q_g \approx 1.67$, this would change the dust mass evolution from $M_{\text{dust}} \propto t^{-0.32}$ for $q_p = 1.87$ to $M_{\text{dust}} \propto t^{-0.40}$ for $q_p = 2.00$. Figure 10 shows the rather moderate dependence of the index ξ on the two mass distribution slopes, q_g and q_p .

While the dust size limit, s_D , has little influence on the mass budget, the breaking size, s_b , the maximum size, s_{max} , and the ratio of the two are relevant to the evolution as they define the lifetime of the largest bodies τ_{max} relative to τ_b . What is more, the ratio s_b/s_{max} determines the rate of the mass decay in equation (39). From § 2.2 we know the location of the breaking radius to be 316 m for the material properties assumed, and the upper size limit of all the runs was set to $s_{\text{max}} = 74$ km.

Another parameter in the analytic model is the collisional lifetime of objects of breaking radius, $\tau_b = \tau(m_b)$. Equation (31) expresses it through other parameters critical for the efficiency of collisions: the radial distance to the star r , the disk radial extension dr , and the effective eccentricity e and inclination I . We choose to fix both the effective distance and the disk extension to be $r = 4/3 dr = 10$ AU when reproducing analytically the results of the ii-0.3 run, 20 AU for i-0.3, 40 AU for o-0.3, and 80 AU for oo-0.3. Further, the inclination can be coupled to eccentricity by assuming the equilibrium condition $I = e/2$. Thus, only e remains as a free parameter. The best fit to, e.g., the ii-0.3 run is achieved if we assume $e \approx 0.075$ in the analytic model, which is approximately one-quarter of $e_{\text{max}} = 0.3$. With these choices, we find $\tau(s_b) \approx 4 \times 10^5$ yr.

Alternatively, τ_b can be directly retrieved from the break in the evolution of the dust mass (see Fig. 9). This method gives

$\tau(s_b) \approx 5 \times 10^5$ yr, which is approximately 4/3 times the value calculated with equation (31). This discrepancy is probably a result of the particle-in-a-box assumptions made by Wyatt et al. (2007a) in derivation of equation (22). We prefer this empirical scaling and thus applied the factor of 4/3 to all analytically estimated timescales in this paper.

5. EVOLUTION OF DISK LUMINOSITY

5.1. Fractional Luminosity for a Given Age

Following Wyatt et al. (2007a), we define the fractional luminosity of dust as

$$f_d \equiv \frac{\sigma_{\text{tot}}}{4\pi r^2}, \quad (45)$$

which assumes that dust grains are blackbodies, absorbing and reemitting all the radiation they intercept. Wyatt et al. (2007a, their eq. [20]) found that there is a maximum possible fractional luminosity f_{max} for a given age, whose value is independent of the initial disk mass but depends on other model parameters such as the distance r of the disk center from the star, its width dr , size of the largest planetesimals D_c , critical fragmentation energy Q_D^* , orbital eccentricity of planetesimals e (with their inclination being $I = e/2$), and the stellar mass M_* and luminosity L_* .

We now wish to explore $f_d(t)$ and check whether it has an upper limit in the framework of our analytic model. To this end, we used equation (45) and calculated σ_{tot} with the aid of our equation (43) for the dust mass. We assumed a solar-type star with $M_* = L_* = 1$ and probed disks with $M_{\text{disk}} = 1, 3, 10,$ and $30 M_\oplus$; $r = 3, 10, 30,$ and 100 AU; $dr/r = \frac{1}{8}, \frac{1}{4}, \frac{1}{2},$ and 1 ; and $e = 0.05, 0.10, 0.15,$ and 0.20 . The results are presented in Figure 11 (*thick lines*). As a standard case, we adopted $M_{\text{disk}} = 10 M_\oplus, r = 30$ AU, $dr/r = \frac{1}{2}$, and $e = 0.10$. It is shown with a thick solid line in each of the panels.

In the same Figure 11, we have overplotted with thin lines the dust luminosity f_d computed with equations (14), (19), and (20) of Wyatt et al. (2007a) for comparison. In that calculation, we assumed $Q_D^* = 300 \text{ J kg}^{-1}$ (constant in their model), $D_c = 60$ km, and the same values of those parameters that are common in their and our model ($M_*, L_*, r, dr/r,$ and e).

Analysis of Figure 11 allows us to make a number of conclusions. First, as expected, our model yields more gently sloping curves than that by Wyatt et al. (2007a). As discussed above, the $1/t$ law will be asymptotically reached in our model, too, but this does rarely happen at ages $t < 10$ Gyr. Only the first signs of the curves’ steepening appear at gigayear ages, and that only for the cases when the collisional evolution is faster (higher masses, closer in or more confined dust rings, higher eccentricities). As a consequence of the slope difference between the two models, our model places more stringent upper limits of f_d at earlier ages, and conversely, it allows the gigayear old systems to have a somewhat higher f_d than the model by Wyatt et al. (2007a) does.

Next, the dependence of f_{max} on the initial disk mass, which cancels out in their model, is retained in our nominal runs (*top left panel*). In fact, the maximum possible f_d is then determined by the maximum initial disk mass that still appears physically plausible in the framework of theories of planetesimal accretion and planet formation.

Another point to mention is that, whereas the dependence on the disk width (*bottom right panel*) and planetesimal eccentricities is relatively weak and monotonic, the dependence on the disk location (*top right panel*) is rather strong and more intricate. That the dependence is strong is the consequence of equation (13), which predicts the timescales to very sensitively depend on the

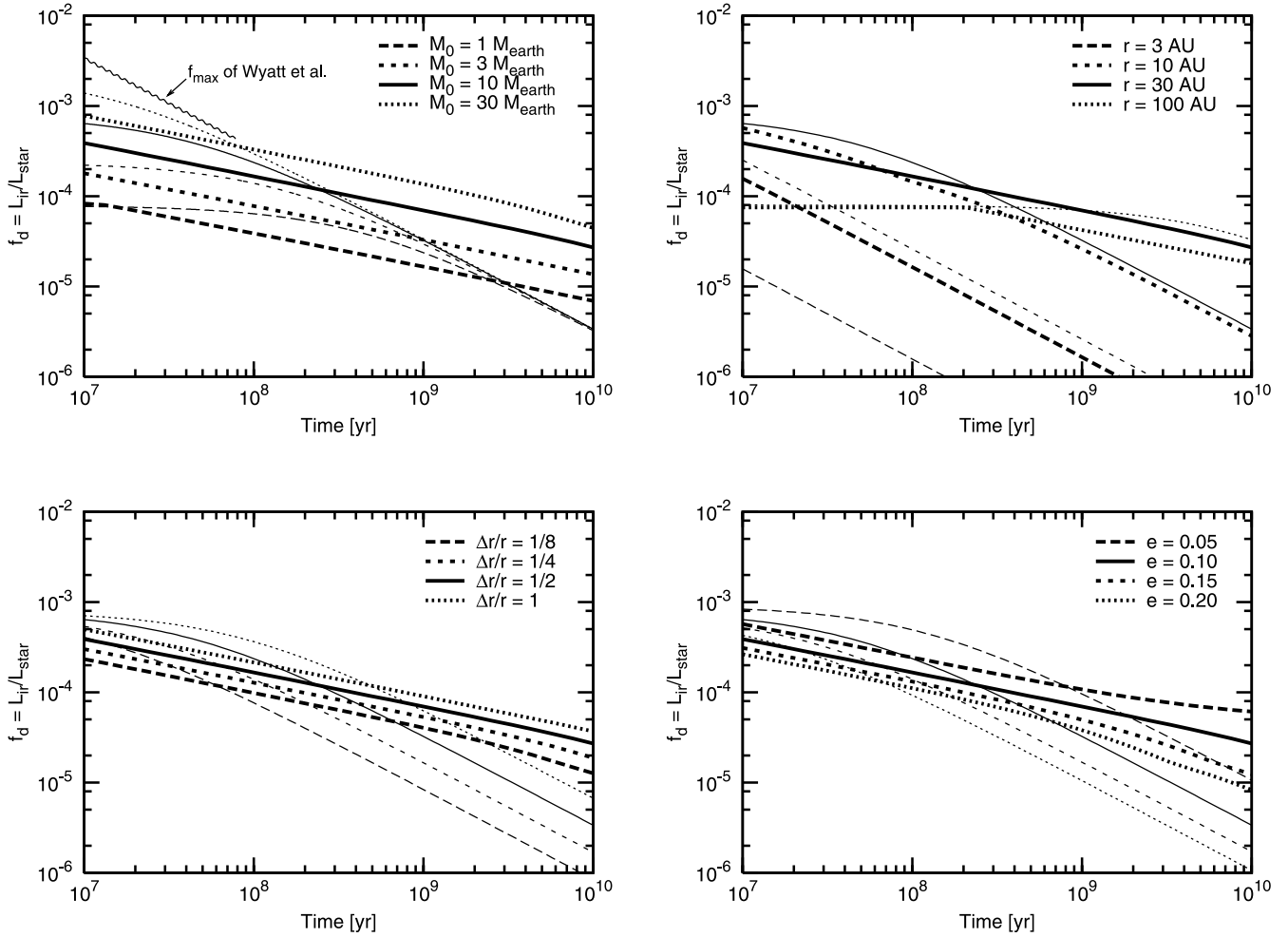


FIG. 11.—Fractional luminosity of dust around a solar-like star as a function of age. *Thick lines*: our analytic model; *thin lines*: f_d of Wyatt et al. (2007a). Different panels demonstrate dependence on different parameters: M_{disk} (top left), r (top right), dr/r (bottom left), and e (bottom right). A standard case with $M_* = L_* = 1$, $M_{\text{disk}} = 10 M_{\oplus}$, $r = 30$ AU, $dr/r = \frac{1}{2}$, and $e = 0.10$ is shown with solid lines (common in all panels).

distance from the star, and of equation (45), which contains a “dilution factor” r^2 . At the beginning of the evolution, the innermost ring is always the brightest because the dilution factor r^2 in equation (45) is the smallest. At the end of the evolution, the opposite is true: the outermost ring will become the brightest because its collisional evolution is the slowest and it retains more mass than inner disks. Therefore, all four curves intersect each other at a certain point; the 30 and 100 AU curves do that after 10 Gyr, i.e., outside the right edge of the plot. After that, all the curves go parallel to each other in the “Dominik-Decin regime,” following a $1/t$ law. Note that inner rings reach the $1/t$ regime more quickly: already at 10 AU it is established in around 100 Myr for an initial mass of $10 M_{\oplus}$.

Although the existence of a “maximum fractional luminosity for a given age,” as suggested by Wyatt et al. (2007a), no longer holds in our model as a robust mathematical statement, in practice our model still suggests that $f_d(t)$ cannot exceed a certain limit, unless the model parameters take extreme values, incompatible with our understanding of the planetesimal disks. For instance, we do expect $f_d < 10^{-4}$ at $t = 10$ Gyr, provided that the initial disk did not contain more than $30 M_{\oplus}$ of solids and that the mean orbital eccentricity of planetesimals is not lower than 0.1 (corresponding to the mean inclination larger than 3°). Therefore, plots such as Figure 11 can be used to check whether or not f_d observed for a certain system with a known age is compatible with a

“smooth,” unperturbed collisional evolutionary scenario. In case it is not, it will be an indication that other mechanisms (delayed stirring, recent giant breakups, noncollisional dust production, etc.) should be thought of to explain the observations.

5.2. 24 and 70 μm Fluxes from Partial Rings

In order to produce directly observable quantities from the derived dust masses, we now concentrate on dust luminosities at particular infrared wavelengths. We calculated the dust temperature and the thermal emission integrated over the whole disk with a more accurate, yet sufficiently simple, model, assuming that the absorption/emission efficiency is constant up to wavelengths of 2π times the size of the particles, s , and proportional to s^{-1} beyond that (Backman & Paresce 1993). Then we computed the spectral flux densities of dust emission F_d and of the stellar radiation F_* at a certain wavelength, as well as their ratio F_d/F_* . As the size distribution in the dust regime quickly reaches its steady state, the luminosity F_d is directly proportional to the dust mass. Therefore, the same initial constancy and subsequent t^ξ decay with $\xi = -0.3$ to -0.4 apply.

Figure 12 shows the evolution of the excess emission at the *Spitzer* MIPS wavelengths 24 and 70 μm , obtained from the four nominal runs. Since all disks have the same initial total mass ($1 M_{\oplus}$), the disks closer to the star are brighter and start to decay earlier. The difference between the excesses at 24 and 70 μm , a

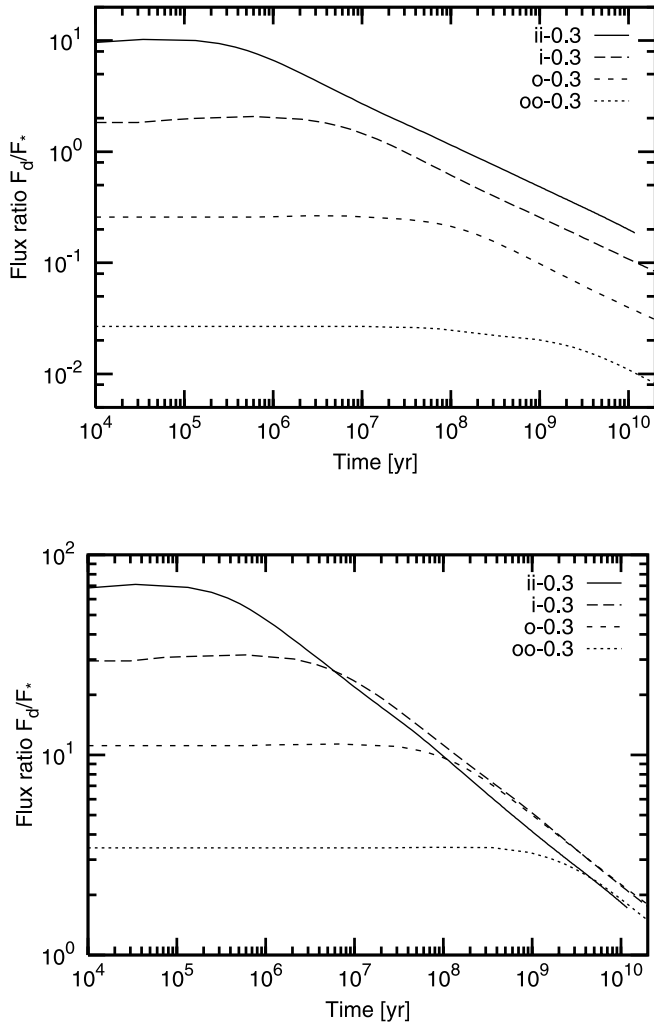


FIG. 12.—Flux ratio vs. time for 24 μm (top) and 70 μm (bottom).

measure of the disks' effective temperature, is varying with radial distance as well. Thus, the convergence of just the 70 μm fluxes at later times is only coincidental. It is a result of the radial dependence of temperature and the collisional timescale.

5.3. Fluxes from Extended Disks

Since resolved debris disks suggest that the parent body reservoir in the disks is usually confined to a toroidal region (a planetesimal belt) or is made up of several such tori, it seems appropriate to simply combine individual rings without taking into account possible interactions between particles that belong to different rings. Thus, we summed up the fluxes from the four main runs. Different radial distributions in the whole disk were simulated by “weighting” the individual rings:

$$F_d = \sum_{j=1}^4 F_{d,j} (r_j/r_0)^\gamma, \quad (46)$$

where r_j are the central distances of the rings and values of 0, 1, 2, and 3 were used for the slope γ . As the reference runs were made for rings of $1 M_\oplus$ each with volumes proportional to r^3 , the corresponding volume density in the extended disk is proportional to $r^{\gamma-3}$, while the pole-on surface density and normal geometrical optical depth follow $\propto r^{\gamma-2}$. The distance r_0 normalizes the total mass to $1 M_\oplus$. Therefore, by changing the slope, the mass is only shifted between inner and outer regions.

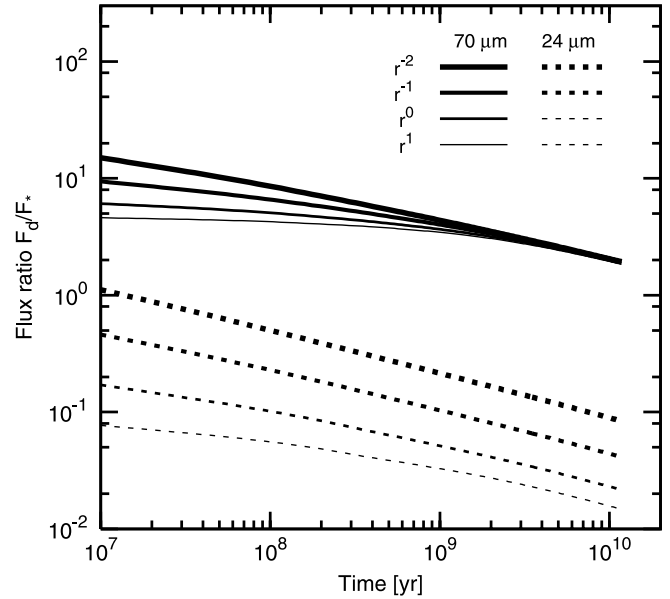


FIG. 13.—Time evolution of the infrared excess of extended disks with different initial radial distributions (labels indicate the radial slope of the surface mass density; the thicker the lines, the flatter the profiles) at 24 μm (dashed lines) and 70 μm (solid lines). The total mass is $1 M_\oplus$ in each case.

In Figure 13 the effect on the 24 and 70 μm fluxes is shown. If the weights are assigned in favor of more distant debris rings, the resulting fluxes are naturally reduced. The same is true for the speed of the decay because the timescales get longer. The evolution of the fluxes at the two *Spitzer* MIPS wavelengths 24 and 70 μm differs significantly. At 24 μm the decay starts earlier and reaches its maximum speed earlier because shorter lived inner regions make the main contribution.

The models contain a sufficient number of parameters, variation of which would affect the curves in Figure 13 in different ways. As stated earlier, varying the total mass changes the timescale according to $\tau \propto M_{\text{disk}}^{-1}$. Hence, the curves can be shifted along the lines of equal tM_{disk} , i.e., along the top left–bottom right diagonal. As seen from Figure 13, variation of the radial distribution changes both the absolute level and the tilt of the curves. Besides, it affects the disk colors, i.e., the separation of the 24 and 70 μm curves in Figure 13. In addition, the dynamical timescales, and therefore the tilt of the curves, are affected by eccentricities and inclinations of the parent bodies that may reflect the presence of planetary perturbers in the disk (see § 3.3). Altogether, these degrees of freedom would allow one to reproduce a broad set of observational data.

6. COMPARISON WITH OBSERVATIONAL DATA

6.1. *Spitzer* Data

The advent of the *Spitzer Space Telescope* has brought a tremendous increase in the number of main-sequence stars surveyed for the existence of cold dust emission (for a recent compilation see Werner et al. 2006).

The wealth of data from these debris disk surveys allows us to confront our models with actual observations. To this end, we searched the literature for published flux ratios at 24 and/or 70 μm (two of the three MIPS bands) around G-type main-sequence stars. To qualify as a main-sequence star, we applied a lower limit to the stellar age of 10 Myr. Sources with stellar age estimates younger than this are likely stars with gas-dominated, protoplanetary disks; these were not taken into account.

The bulk of the data taken in the framework of the Legacy program “Formation and Evolution of Planetary Systems” (FEPS; Meyer et al. 2004, 2006) are public since 2006 December. The FEPS archive contains images, spectra, photometry tables, and Kurucz photosphere models and is available online.¹ Age estimates have been published for 46 FEPS G stars (Kim et al. 2005; Stauffer et al. 2005; Silverstone et al. 2006).

The large Guaranteed Time Observer (GTO) survey of FGK stars contains another 64 stars, where ages are available (Beichman et al. 2005, 2006b; Bryden et al. 2006). Data for 10 more G stars are listed in Chen et al. (2005a, 2005b). In total, 120 G-type main-sequence stars with flux ratios at 24 and/or 70 μm have been compiled from the literature for comparison with model flux ratios.

6.2. Population Synthesis

Based on the analytic prescription presented in § 4 and motivated by the Wyatt et al. (2007b) work, we now build a synthetic set of debris disks around G2 stars. We generate a set of ringlike disks of width dr located at distances $r \in [r_{\min}, r_{\max}]$, with masses $M_{\text{disk}} \in [M_{\min}, M_{\max}]$ and ages between 10 Myr and 10 Gyr. The probability to have a disk of initial mass M_0 at radius r was assumed to follow $M_0^{-1} r^{-0.8}$, where M_0^{-1} corresponds to a log-normal distribution of initial disk masses and the $r^{-0.8}$ dependence was proposed by Wyatt et al. (2007b). As described in § 5.2, the temperatures and the resulting thermal fluxes are calculated using the modified blackbody formulae by Backman & Paresce (1993) assuming the emitting grains to have $s = 1 \mu\text{m}$, in agreement with the size distribution shown in Figure 4. The other parameters are taken to be $q_p = 2.00$, $q_g = 1.67$, $q_s = 1.877$, $dr/r = 0.5$, $2I = e = 0.15$, $Q_D^*(1 \text{ m}) = Q_D^*(1 \text{ km}) = 5 \times 10^6 \text{ ergs g}^{-1}$, $b_D = -0.12$, $b_g = 0.47$, roughly corresponding to basalt in Benz & Asphaug (1999).

Due to the small observational sample, our aim was not to perform a multiparameter fit to the observations, but rather to cover the range of observed flux densities, which is defined by the limits of the distributions, not by their slopes.

Varying disk locations and masses easily reproduces the observed distribution of fluxes at 24 and 70 μm (Fig. 14). The synthetic population shown corresponds to $r_{\min} \approx 20 \text{ AU}$, $r_{\max} \approx 120 \text{ AU}$ and $M_{\min} < 0.01 M_{\oplus}$, $M_{\max} \approx 30 M_{\oplus}$. Here the radial range is needed to cover the range of colors, i.e., the ratios between the excess emissions at the two wavelengths. The mass range is needed to cover the observed range of excess, especially for younger disks at 70 μm .

Analyses of *Spitzer* detections might indicate a statistically significant increase of both 24 and 70 μm fluxes at ages between a few tens and a few hundreds of megayears (e.g., J. M. Carpenter et al. 2008, in preparation), which can only be marginally seen in our sample (Fig. 14). It is hypothesized that this feature is caused either by an increased dust production due to delayed stirring by growing planets or by events similar to the late heavy bombardment in the solar system. Such effect could only be studied with an improved version of our analytic model or with the numerical one.

The distribution of disk colors is more difficult to reproduce. Figure 15 shows a significant abundance of fainter but warmer disks in an area that is not covered by the synthetic population. One explanation would be that the upper mass limit is a function of radial distance, and that the innermost disks tend to be less massive and less luminous, from the very beginning. In addition, the bottom panel of Figure 15 shows a trend toward higher effective temperatures for higher ages, which is difficult to understand. Indeed, as

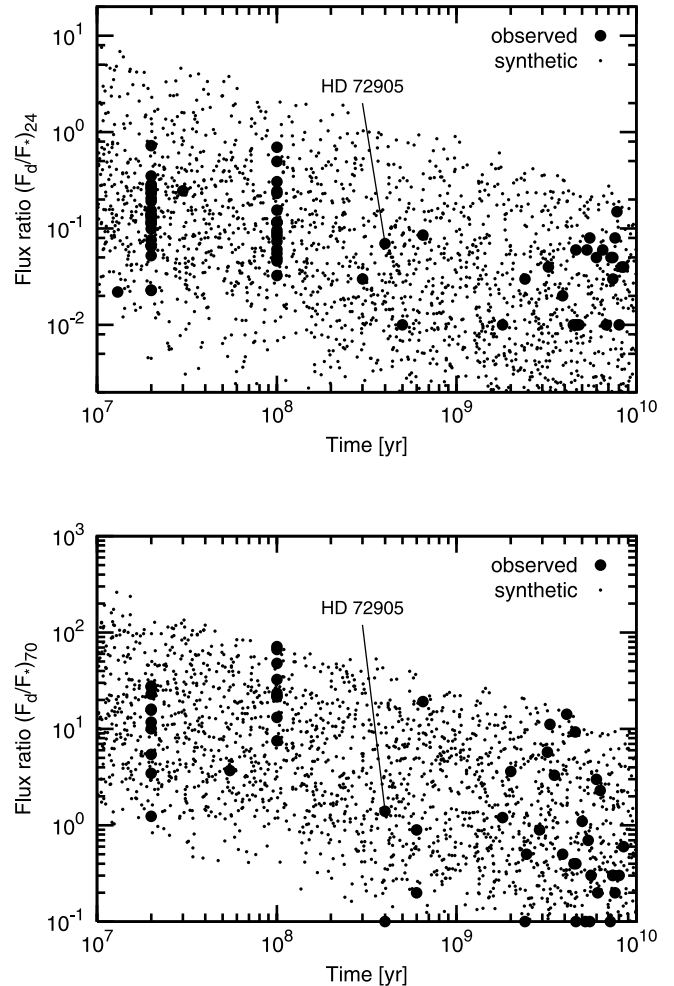


FIG. 14.—Flux ratios vs. time for 24 μm (top) and 70 μm (bottom). The synthesized population (small filled circles) is compared to the observed one (large filled circles). Individually labeled is the possibly transient system HD 72905; see text.

long as faint close-in disks are observed around older stars, one would expect ever brighter disks, and therefore more numerous detections of disks at the same distances around younger stars. Furthermore, the trend in question contradicts the results by Najita & Williams (2005), who found no significant correlation between the disk radii and ages. Most likely, the discrepancy is only caused by uncertainties of the measured excesses at 24 μm . Bryden et al. (2006) report that the average photometric accuracy in that filter band is only as good as $1\sigma_{24} = 6\%$ due to stellar photosphere fitting errors and flat-field uncertainties. Therefore, excesses below those 6% of the photospheric emission cannot be considered as significant. For 70 μm , Bryden et al. (2006) state $1\sigma_{70} \approx 15\%$. Both limits are shown in the top panel of Figure 15.

In Figures 14 and 15, there is one particular system directly labeled. That system, HD 72905, was observed to show significant excess emission not only at 24 and 70 μm but also in the spectral ranges 8–13 μm and 30–34 μm of the *Spitzer* IRS instrument (Beichman et al. 2006a). The presence of two dusty regions was suggested: one exozodiacal at 0.03–0.43 AU and one around 14 AU. From the excess at 8–13 μm , Wyatt et al. (2007a) inferred the dust population in HD 72905 to be transient because the observed fractional luminosity is above the maximum expected for a system of 300–400 Myr. As long as only 24 and 70 μm are considered, the HD 72905 dust does not seem particularly hot or bright, although it is among the hotter disks.

¹ See http://data.spitzer.caltech.edu/popular/feps/20061223_enhanced_v1.

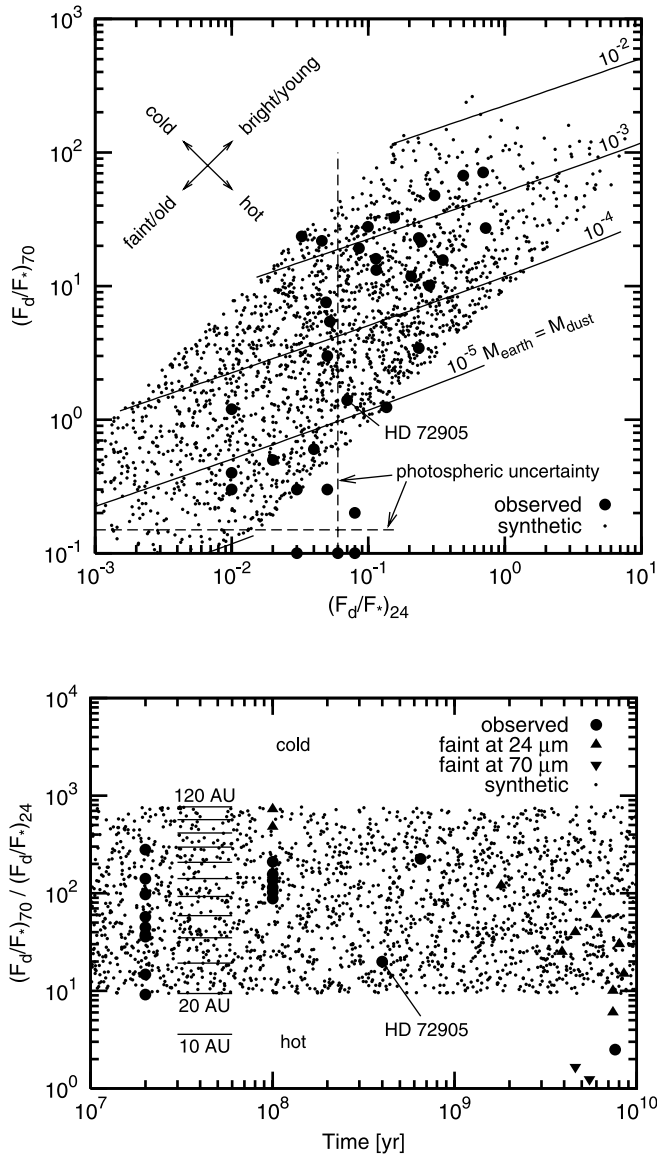


FIG. 15.—Relation between fluxes at 24 and 70 μm vs. time. The synthesized population (small filled circles) is compared to the observed one (large filled circles and triangles). The average photospheric uncertainty for both filters is marked by dashed lines in the top panel. Excesses below those limits in either of the two filters are marked by triangles in the bottom panel. In addition, the top panel shows lines of equal dust mass, and the bottom panel gives the ring radii corresponding to the colors.

At this point, it is interesting to compare our results to those of Wyatt et al. (2007b). Both analytic approaches aim at explaining and reproducing the observations. Our model is different from theirs in that we take into account the size dependence of the critical specific energy, as well as the transition from a primordial size distribution of planetesimals to the one set up by a collisional cascade. The amount of dust in their model is determined, from the very beginning, by the rather long collisional timescales of objects of tens of kilometers, so that the collisional evolution is much slower. This can be seen from the equations: “1+” in the denominator of equation (10) causes the mass to stay almost at the initial level for a long time, before the system reaches the t^{-1} decay. In our model, although the mass decay is asymptotically slower (t^ξ with $\xi \approx -0.3$ to -0.4), it sets up very quickly, namely, on collisional timescales of objects with minimum binding energy ($s_b \sim 100$ m). Therefore, we would expect the model by Wyatt et al. (2007b) to show significantly larger excesses at ages con-

sidered, if all other parameters were comparable. This, however, is not the case. Wyatt et al. (2007b) assumed a much weaker material in their collisional prescription. Their $Q_D^* = 300 \text{ J kg}^{-1}$ at an object radius of 30 km ($D_c = 60$ km) is by more than 2 orders of magnitude below the values we use in equation (1). As $\tau \propto Q_D^{q_p-1}$ in equation (34), their collisional timescales are shorter and their evolution faster, too. Besides the material strength, the difference in the assumed effective eccentricities— $e = 0.05$ in their model against $e_{\text{max}}/2 = 0.15$ in ours—causes another factor of roughly 10 in the collisional timescales, according to § 3.3. All the differences listed happen to nearly compensate each other. As a net result, the excesses predicted by our model and that of Wyatt et al. (2007b) are comparable with each other (see also Fig. 11), being in reasonable agreement with the observed ones.

7. SUMMARY AND CONCLUSIONS

We investigated the long-term evolution of debris disks around solar-type (G2 V) stars. First, we performed numerical simulations with our collisional code. Second, the numerical results were supplemented by, and interpreted through, a new analytic model. The latter is similar to, and builds on, the model developed earlier by Wyatt et al. (2007a) but extends it in several important directions. It naturally includes the transition from the primordial size distribution of leftover planetesimals, set up at their agglomeration phase, to the size distribution established by the collisional cascade. Further, it lifts the assumption that the critical specific energy needed for disruption is constant across the full range of sizes, from dust to the largest planetesimals. With these improvements, a good agreement between the numerics and analytics is achieved.

We draw the following conclusions:

1. The timescale of the collisional evolution is inversely proportional to the initial disk mass. For example, halving the total mass doubles all collisional timescales. This rule is valid for systems where collisions are the only loss mechanism of particles and only as long as β -meteoroids are unimportant for the collisional budget.
2. Numerics and analytics consistently yield a $\tau \propto r^{4.3}$ dependence of the timescale of the collisional evolution on the radial distance.
3. Numerical simulations show that the collisional timescale varies with the average eccentricity of dust parent bodies as $\tau \propto e^{-2.3}$. The analytic approach suggests a somewhat weaker dependence, $\tau \propto e^{-5/3}$.
4. An evolving three-slope size distribution is proposed to approximate the numerical results. The biggest objects are still distributed primordially, with a slope q_p . The objects below a certain transitional size are already reprocessed by collisions and thus have a quasi-steady state size distribution, determined by their self-gravity (for intermediate-sized objects, slope q_g) or by material strength (for smallest objects, slope q_s). That transitional size corresponds to the largest objects for which the collisional lifetime is still shorter than the age of the system. The transitional size increases with time, meaning that ever larger planetesimals get involved in the collisional cascade.
5. At actual ages of debris disks, ~ 10 Myr to ~ 10 Gyr, the decay of the dust mass and that of the total disk mass follow *different* laws. The reason is that, in all conceivable debris disks, the largest planetesimals have longer collisional lifetimes than the system’s age and therefore did not have enough time to reach collisional equilibrium. If the system were let to evolve for a sufficiently long time, both dust mass and disk mass would start to follow t^{-1} . However, this requires time spans of much longer than 10 Gyr.
6. The loss rate of the dust mass and the decay rate of fractional luminosity primarily depend on the difference between the

slope q_p of the primordial size distribution of largest planetesimals and the slope q_g of the size distribution of somewhat smaller, yet gravity-dominated, planetesimals that already underwent sufficient collisional evolution. With “standard” values of q_p and q_g , the dust mass and the thermal fluxes follow approximately t^ξ with $\xi = -0.3$ to -0.4 .

7. Specific decay laws of the total disk mass and the dust mass largely depend on a few model parameters. Most important are the critical fragmentation energy Q_D^* as a function of size, the slope of the primordial size distribution of planetesimals q_p and their maximum size s_{\max} , and the characteristic eccentricity e and inclination I of planetesimals.

8. The property that the maximum possible dust luminosity for a given age does not depend on the initial disk mass, established by Wyatt et al. (2007a), is only valid in cases of very rapid collisional evolution, i.e., in closer in or dynamically very hot disks. For most of the systems at ages < 10 Gyr, an increase of the initial disk mass leads to an increase of the dust luminosity, unless that initial mass is assigned extreme values, incompatible with our understanding of planetesimal disks.

9. Assuming standard material prescriptions and disk masses and extents, a synthetic population of disks generated with our analytic model generally agrees with the observed statistics of 24 and 70 μm fluxes versus age. Similarly, the synthetic [24]–[70] colors are consistent with the observed disk colors.

As every model, our numerical model makes a number of general simplifying assumptions; the analytic one imposes further simplifications:

1. The collisional evolution is assumed to be smooth and unperturbed. Singular episodes like the aftermath of giant breakups or special periods of the dynamical evolution such as the late heavy bombardment are not included.

2. Effects of possible perturbing planets are taken into account only indirectly: through the eccentricities of planetesimals (dynamical excitation) and confinement of planetesimal belts (truncation of disks). Further effects such as resonant trapping or ejection of material by planets are neglected.

3. We only consider disruptive collisions. This is a reasonable approximation for disks that are sufficiently “hot” dynamically. However, cratering collisions become important when the relative velocities are insufficient for disruption to occur.

4. Neither dilute disks under the regime of Poynting-Robertson drag nor very dense disks with collisional timescales shorter than orbital timescales and with avalanches (Grigorieva et al. 2007) are covered by the present work.

5. Explaining the initial conditions or deriving them from the dynamical history of the systems at early stages of planetesimal and planetary accretion was out of the scope of this paper. Correlations between disk masses, disk radii, and the presence of planets, for example, were not considered, although they might alter the scalings we found here.

Despite these limitations, our models reproduce, in essential part, the observed evolution of dust in debris disks. We hope that they may serve as a starting point for in-depth studies that will certainly be undertaken in the future, motivated by questions that remain unanswered, as well as by new data expected from ongoing and planned observational programs.

We wish to thank Jean-François Lestrade Philippe Thébault, and Mark Wyatt for fruitful discussions and Amaya Moro-Martín for useful review comments. This research has been partly funded by the Deutsche Forschungsgemeinschaft (DFG), project Kr 2164/5-1.

REFERENCES

- Artymowicz, P. 1997, *Annu. Rev. Earth Planet. Sci.*, 25, 175
 Augereau, J., & Beust, H. 2006, *A&A*, 455, 987
 Aumann, H. H., et al. 1984, *ApJ*, 278, L23
 Backman, D. E., & Paresce, F. 1993, in *Protostars and Planets III*, ed. E. H. Levy & J. I. Lunine (Tucson: Univ. Arizona Press), 1253
 Beichman, C. A., et al. 2005, *ApJ*, 622, 1160
 ———. 2006a, *ApJ*, 639, 1166
 ———. 2006b, *ApJ*, 652, 1674
 Benz, W., & Asphaug, E. 1999, *Icarus*, 142, 5
 Bernstein, G. M., et al. 2004, *AJ*, 128, 1364
 Bryden, G., et al. 2006, *ApJ*, 636, 1098
 Campo Bagatin, A., Cellino, A., Davis, D. R., Farinella, P., & Paolicchi, P. 1994, *Planet. Space Sci.*, 42, 1079
 Chen, C. H., Jura, M., Gordon, K. D., & Blaylock, M. 2005a, *ApJ*, 623, 493
 Chen, C. H., et al. 2005b, *ApJ*, 634, 1372
 ———. 2006, *ApJS*, 166, 351
 Davis, D. R., & Ryan, E. V. 1990, *Icarus*, 83, 156
 Dohnanyi, J. W. 1969, *J. Geophys. Res.*, 74, 2531
 Dominik, C., & Decin, G. 2003, *ApJ*, 598, 626
 Durda, D. D., & Dermott, S. F. 1997, *Icarus*, 130, 140
 Fujiwara, A. 1986, *Mem. Soc. Astron. Italiana*, 57, 47
 Fujiwara, A., Kamimoto, G., & Tsukamoto, A. 1977, *Icarus*, 31, 277
 Gorlova, N., et al. 2006, *ApJ*, 649, 1028
 Greaves, J. S. 2005, *Science*, 307, 68
 Greaves, J. S., & Wyatt, M. C. 2003, *MNRAS*, 345, 1212
 Grigorieva, A., Artymowicz, P., & Thébault, P. 2007, *A&A*, 461, 537
 Jura, M., et al. 2004, *ApJS*, 154, 453
 Kenyon, S. J., & Bromley, B. C. 2004, *AJ*, 128, 1916
 Kim, J. S., et al. 2005, *ApJ*, 632, 659
 Krivov, A. V., Löhne, T., & Sremčević, M. 2006, *A&A*, 455, 509
 Krivov, A. V., Mann, I., & Krivova, N. A. 2000, *A&A*, 362, 1127
 Krivov, A. V., Sremčević, M., & Spahn, F. 2005, *Icarus*, 174, 105
 Laor, A., & Draine, B. T. 1993, *ApJ*, 402, 441
 Lestrade, J.-F., Wyatt, M. C., Bertoldi, F., Dent, W. R. F., & Menten, K. M. 2006, *A&A*, 460, 733
 Liu, M. C., Matthews, B. C., Williams, J. P., & Kalas, P. G. 2004, *ApJ*, 608, 526
 Matthews, B. C., et al. 2007, *PASP*, 119, 842
 Meyer, M. R., et al. 2004, *ApJS*, 154, 422
 ———. 2006, *PASP*, 118, 1690
 Michel, P., Tanga, P., Benz, W., & Richardson, D. C. 2002, *Icarus*, 160, 10
 Moór, A., et al. 2006, *ApJ*, 644, 525
 Najita, J., & Williams, J. P. 2005, *ApJ*, 635, 625
 O’Brien, D. P., & Greenberg, R. 2003, *Icarus*, 164, 334
 Pan, M., & Sari, R. 2005, *Icarus*, 173, 342
 Paolicchi, P., Verlicchi, A., & Cellino, A. 1996, *Icarus*, 121, 126
 Rieke, G. H., et al. 2005, *ApJ*, 620, 1010
 Silverstone, M. D., et al. 2006, *ApJ*, 639, 1138
 Spangler, C., Sargent, A. I., Silverstone, M. D., Becklin, E. E., & Zuckerman, B. 2001, *ApJ*, 555, 932
 Stauffer, J. R., et al. 2005, *AJ*, 130, 1834
 Strubbe, L. E., & Chiang, E. I. 2006, *ApJ*, 648, 652
 Su, K. Y. L., et al. 2006, *ApJ*, 653, 675
 Tanga, P., et al. 1999, *Icarus*, 141, 65
 Tedesco, E. F., Cellino, A., & Zappalá, V. 2005, *AJ*, 129, 2869
 Thébault, P., & Augereau, J.-C. 2007, *A&A*, 472, 169
 Thébault, P., Augereau, J. C., & Beust, H. 2003, *A&A*, 408, 775
 Trujillo, C. A., Jewitt, D. C., & Luu, J. X. 2001, *AJ*, 122, 457
 Werner, M., Fazio, G., Rieke, G., Roellig, T. L., & Watson, D. M. 2006, *ARA&A*, 44, 269
 Wyatt, M. C. 2005, *A&A*, 433, 1007
 Wyatt, M. C., et al. 2007a, *ApJ*, 658, 569
 ———. 2007b, *ApJ*, 663, 365